https://doi.org/10.1016/j.nanoen.2023.108380

Atomic phosphorus induces tunable lattice strain in high entropy alloys and boosts alkaline water splitting

Qiao Chen,[‖,†] Xiao Han,[‖,†,⊥,] Ziyuan Xu, [‖,†] Qingxi Chen,[†] Qingfeng Wu,[†] Tao Zheng,[†] Pan Wang,[†] Zhijun Wang,[†] Jincheng Wang,[†] Hejun Li,[†] Zhenhai Xia,[§,*] Jianhua Hao[⊥,*]*

[†]State Key Laboratory of Solidification Processing, School of Materials Science and Engineering, Northwestern Polytechnical University, Xi'an, 710072, P.R. China

[§]Department of Materials Science and Engineering, Department of Chemistry, University of North Texas, Denton, TX, 76203, USA

[⊥]Department of Applied Physics, The Hong Kong Polytechnic University, Hong Kong, P.R. China

[*]Email: xiao.han@nwpu.edu.cn (X. Han)

Zhenhai.xia@unt.edu (Z. Xia)

jh.hao@polyu.edu.hk (J. Hao)

[‖]These authors contributed equally to this work.

Abstract

High entropy alloys (HEAs) recently emerges as a potential platform to construct multifunctional electrocatalysts owing to their unique inherent complexity. Herein, a strain engineering strategy is reported to design and fabricate P-doped porous HEA electrodes with tunable heteroatom loadings and lattice strains, thus tailoring the intrinsic electronic structure and boosting the catalytic properties of HEA. Instead of forming phosphides, graded distribution of tensile strain is observed in the porous HEA after P doping, as confirmed by various experimental measurements and the first-principles calculation results. Benefiting from the introduction of heteroatoms and the induced lattice strain, the exposed electrocatalytic active area and intrinsic specific activity of P-doped porous HEA have been greatly enhanced in the meantime. As a result, the obtained 1P-HEA electrode exhibited excellent alkaline hydrogen and oxygen evolution reaction activity, requiring low overpotentials of 70 mV and 211 mV at 10 mA cm^{-2}, respectively. Additionally, a full water splitting electrolyzer constructed based on bifunctional 1P-HEA electrodes outperforms commercial Pt/C and RuO_2 counterparts and remains almost 100% activity after continuous 84 h of stability testing at an ultrahigh current density of 2 A cm^{-2} under simulated industrial condition.

Introduction

The exhaustion of fossil fuels arouses considerable research interest in exploring novel types of alternative energy and efficient energy storage systems[1,2]. Electrochemical water splitting is one of the most promising strategies to produce high-purity hydrogen, which shows high potential as sustainable energy to convert the stored chemical energy to electrical energy with high energy density and environmentally friendly products[3,4]. Due to the sluggish reaction kinetics, highly efficient electrocatalysts are normally required to lower the activation barrier and boost the reaction process[5–7]. Commercially, the utilization of noble metal-based catalysts is common, for example, Pt for hydrogen evolution reaction (HER), RuO_2 or IrO_2 for oxygen evolution reaction (OER). However, electrochemical water splitting is still hindered by several knotty problems: the high overpotential, slow kinetics, short operation lifespan of electrodes, and the high price of noble-metal catalysts[8–10].

Currently, the state-of-the-art non-noble-metal electrocatalysts to split water in alkaline electrolyte are mostly based on transition-metal oxides[11], chalcogenides[12], nitrides[13], and phosphides[14]. However, the limited electroactive sites and insufficient stability seriously restricted their further practical applications[15]. Moreover, numerous researches have demonstrated that automatic structural reconstruction occurred on the surface of the above electrocatalysts while performing as OER electrodes. In this regard, these electrocatalysts under non-reaction conditions should be called “pre-catalysts” rather than the “true catalyst”[16,17]. Up to date, the construction of a high-performance “true catalyst” with long-term stability remains a challenge.

Benefiting from their tunable composition and tailoring of functional properties, high-entropy alloys (HEAs) have attracted tremendous attention in many fields[18], including the rapidly growing investigations for electrocatalysis in the past three years. Due to the inherent complexity, the local coordination environment and electronic structure can be adjusted, thus the adsorption energy of intermediates on HEAs can be optimized attributing to the change of orbital overlap. As a consequence, HEAs possess various electro-catalytic active sites and extremely high mechanical properties, performing as a perfect platform to be further modified with diversified adsorption sites and tunable

electronic structure, compared to traditional transitional metals or binary alloys[19]. Recently, although blossoming studies on transition-metal alloying have been reported, there are few studies on modifying the electrocatalytic activity of HEA catalysts by as-introduced hetero-anion atoms[10,18,20]. As an effective modifying strategy, surface anion decoration is beneficial for optimizing the electronic structure along with the absorption energy of the intermediates thus greatly accelerating water dissociation. Despite the traditional anion doping process upon transition metals tends to form their compounds (oxides, chalcogenides, nitrides, and phosphides) which usually deteriorate rapidly under anodic oxidation conditions [16,21], the interaction between HEA and hetero-anion atoms is not fully investigated.

Herein, a monolithic porous HEA electrode for overall water splitting with adjustable lattice distortion has been successfully constructed via an atomic doping route, and the influences of dopant P on the lattice expansion and electrocatalytic performance are investigated systematically. Atomic lattice strains along with doped P atoms are generated in the as-constructed xP-HEAs due to the temporary high pressure under the sealed environment. The induced lattice expansion and internal strain are unevenly distributed in the porous HEA, as confirmed by high angle annular dark field scanning transmission electron microscopy (HAADF-STEM) and geometry phase analysis (GPA), high-resolution transmission electron microscopy (HRTEM), X-ray diffraction (XRD) patterns, Raman spectra, and first-principles calculations. Consequently, the optimal 1P-HEA electrode, with the highest doping content (2.88 at%) and largest lattice strain (1.13%), presents a low overpotential of 70 and 211 mV at 10 mA cm^{-2} for HER and OER, respectively. Notably, the as-constructed P-doped porous HEA electrodes exhibit impressively structural and catalytic stability during the long-term electrochemical measurement under an ultrahigh current density of 2 A cm^{-2}, showing that the 1P-HEA electrode performs as an ultra-stable electrode throughout overall water splitting process. A combination of experimental characterization and theoretical calculations confirms the significant role of P doping-induced lattice strain in HEA, and the results demonstrate a remarkable improvement in electrocatalytic performance.

Results and discussions

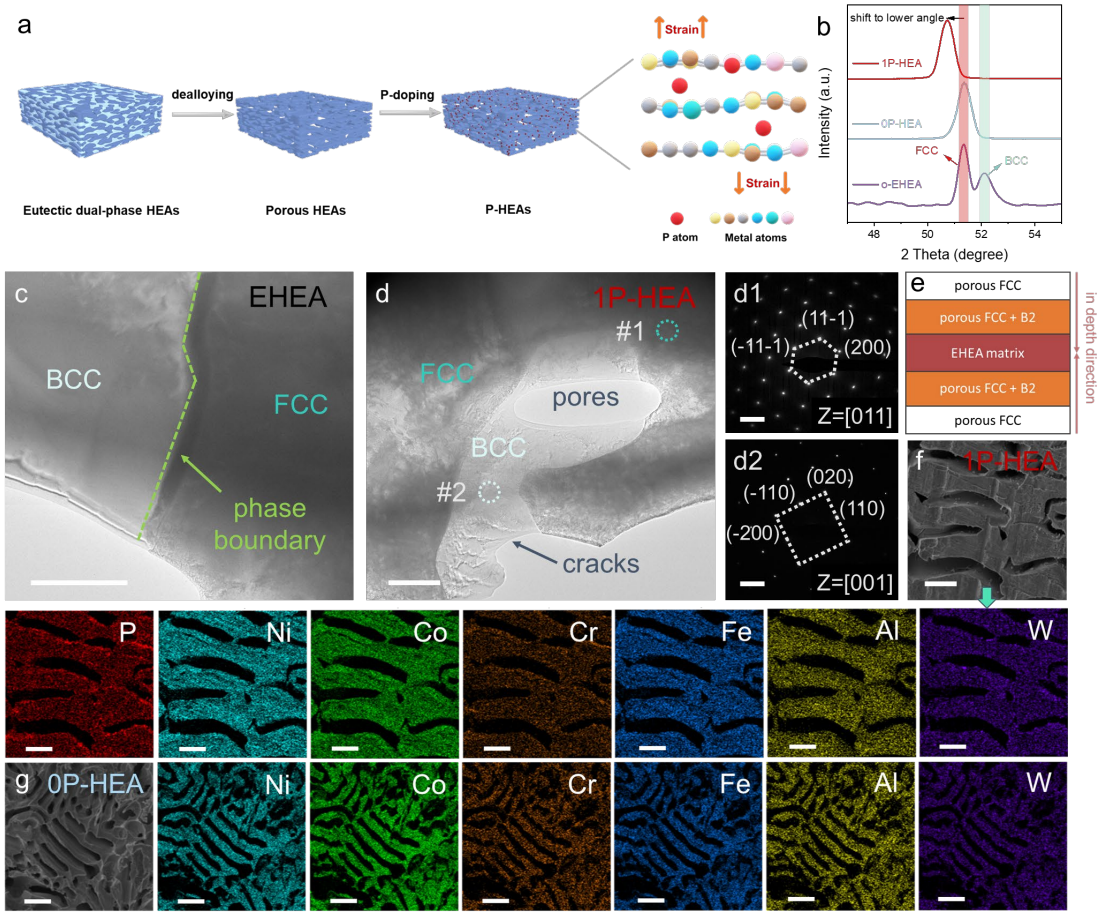

Figure 1. Structural and compositional characterizations of P-doped HEA. (a) Schematic for synthesizing P-HEA and inducing lattice strain. (b) Partial XRD patterns of eutectic high-entropy alloy (EHEA), 0P-HEA, and 1P-HEA. HAADF images of (c) EHEA, and (d) 1P-HEA, the scale bars are 1 μm; and the corresponding selected area electron diffraction (SAED) patterns of (d1) FCC and (d2) BCC phase, the scale bars are 5 nm^{-1}. (e) Illustration of the structure of the 1P-HEA electrode. Scanning electronic microscopy (SEM) images, and their corresponding energy-dispersive spectroscopy (EDS) mapping of (f) 1P-HEA and (g) 0P-HEA, the scale bars are 10 and 20 μm, respectively.

Alloying and defect strategies are proven to be efficient methods to adjust intermediate absorption energy and thus regulate electrocatalytic activity. On this basis, strain-rich xP-HEAs electrodes were fabricated by a two-step method, and the entire construction process is schematically illustrated in Figure 1a. First of all, the eutectic dual-phase

HEA with a nominal composition of $Ni_{30}Co_{30}Fe_{10}Cr_{10}Al_{18}W_2$ is prepared after computational-assisted compositional selection and structural design[22][23], and the specific microstructure and composition are determined by the SEM (Figure S1-S4), TEM (Figure 1c and S5) and inductively coupled plasma optical emission spectrometer (ICP-OES) results (Table S1-S2). Then, along with the selective removal of the B2 phase (Figure 1b) through a facile acid leaching route, porous HEA with a hierarchical structure was obtained, termed as 0P-HEA, and the enriched pores and change of content is distinguished by the SEM (Figure S6), HAADF-EDS (Figure S7) and ICP-OES results. Theoretically, porous HEA, owing to its tunable intermediate absorption energy and sufficient exposed surface area, is expected to exhibit excellent performance for electro-catalytic water splitting. However, porous HEA performs poor HER and ordinary OER activities, thus it is imperative to explore an appropriate method to further boost the inherent catalytic activity of HEA, for example, doping with p-block elements (N, O, S, P, et al.) in the periodic table.

Herein we choose P as a demonstration due to the enhanced performance of P-doped unitary or binary metallic catalysts previously reported. Normally, transition-metal phosphides (TMPs) could be formed at a temperature ranging between 300 and 350 °C[24]. However, due to the intrinsic thermal phase stability of HEA, the general up-down-stream strategy could not induce coordination of PH_3 and porous HEA to form TMPs[25]. Inspired by the carburization technology in the conventional metallurgical process[26], a novel strain engineering strategy achieved by introducing heteroatom doping is adopted to modulate the bulk HEA electrocatalytic activity. Specifically, P-doped porous HEAs, termed as xP-HEAs (x = 0.5, 1, 1.5, 2, equal to the amount of NaH_2PO_2 precursor in gram) were obtained by calcination of the sealed crucible which contains NaH_2PO_2 and porous HEA substrate. Interestingly, the as-constructed P-doped HEAs maintains the surficial single FCC and inner eutectic structure inherited from the porous HEA but with a negative shift on its FCC//(111) peak (Figure 1b), suggesting the existence of P-doping induced tensile strain, which will be elaborated in detail later. And the even distribution of dopant P and other metal elements was confirmed by the atomic-scale HADDF and corresponding elemental mapping (Figure S8).

To investigate the influence of gas pressure and the amount of P sources on the formation mechanism of the P-HEA, the calcination processes with different NaH_2PO_2 additions are studied. SEM images and EDS mapping (Figure S9) results reveal the successful introduction of P in all xP-HEAs, among which 1P-HEA sample with 1 gram NaH_2PO_2 was added possesses the highest doping level of approximately 3.34 at%. Besides, along with NaH_2PO_2 addition, dopant P content in P-HEA changes nonlinearly, which is also in accord with the ICP-OES results (Table S2). The order of P content in xP-HEAs is: 1P-HEA (2.88 at%) > 1.5P-HEA (2.23 at%) > 2P-HEA (1.91 at%) > 0.5P-HEA (1.27 at%), which presents a volcano shape with precursor NaH_2PO_2 amount rather than keeps a linear relation (Figure S10). The reason could be that the redundant sodium phosphate may block the pores in the porous HEA, which are vital pathways for the diffusion and reaction between PH_3 and HEA matrix, thus forming a low P content.

Moreover, HAADF images (Figure 1d) and its corresponding SAED patterns of 1P-HEA were acquired, and the results show that there is no obvious phase transformation or separation after P doping. And the inherited eutectic dual phases consisting of FCC (Figure 1d-1) and residual B2 phase (Figure 1d-2) can be verified by the SAED patterns. The surface of 1P-HEA was also characterized by TEM (Figure S11), and a single crystal structure of FCC phase could be observed. To further testify the existence of P in 1P-HEA, different samples from 1P-HEA in various depths (0, 50, 100, and 150 μm) were obtained through ion thinning. The clear layered phase and graded distribution of P are observed in Figure S12-S13, and an illustration of the structure of 1P-HEA was depicted in Figure 1e. There are three major regions: single FCC mainly existed on the surface of 1P-HEA (with a depth range from 0 to 50 μm), and the co-existence of FCC and residual B2 in the deeper region (from 50 to 100 μm) while the deepest area is intact EHEA (from 100 to 150 μm) without corrosion. From the SEM images of 1P-HEA in Figure 1f-g and Figure S14, it could be easily found that hierarchically porous structure and elemental distribution are well kept during the annealing process. In terms of composition, species including Ni, Co, Cr, Fe, Al, and W were inherited from porous HEA, and the P element was introduced by the P doping process.

X-ray photoelectron spectroscopy (XPS) measurement was conducted to characterize its surface compositions and chemical environments for different species, as shown in Figure S15. For the high-resolution XPS of the 1P-HEA sample at P 2p region, two main peaks for P-M and P-O located at 130.1 and 133.4 are observed, suggesting the formation of metal-phosphorous bonding[27]. However, there is no metal phosphide phase being examined by XRD (Figure 1b) and HRTEM (Figure 1d), which indicates the unique feature of HEA compared to conventional unitary metals and binary alloys. The O 1s XPS spectra of 1P-HEA and 0P-HEA consist of single peak, which was attributed to metal-oxygen bonding[28] and located at 532.4 and 531.7 eV, respectively. The positive shift of O-M bonding indicates the P-induced weakened M-O interaction. Notably, the binding energies of Ni 2p and Co 2p for 1P-HEA exhibit a negative shift compared with that of 0P-HEA, while the peaks attributed to Fe 2p, Cr 2p, Al 2p, and W4f are observed to shift to higher binding energies. The positive shift in the XPS binding energies corresponds to a reduction in charge density around the metal atoms and the negative shift suggests an increase in charge density[29]. This result implies that the local electronic structure and interatomic interactions of 0P-HEA and 1P-HEA have been evidently altered due to the P doping.

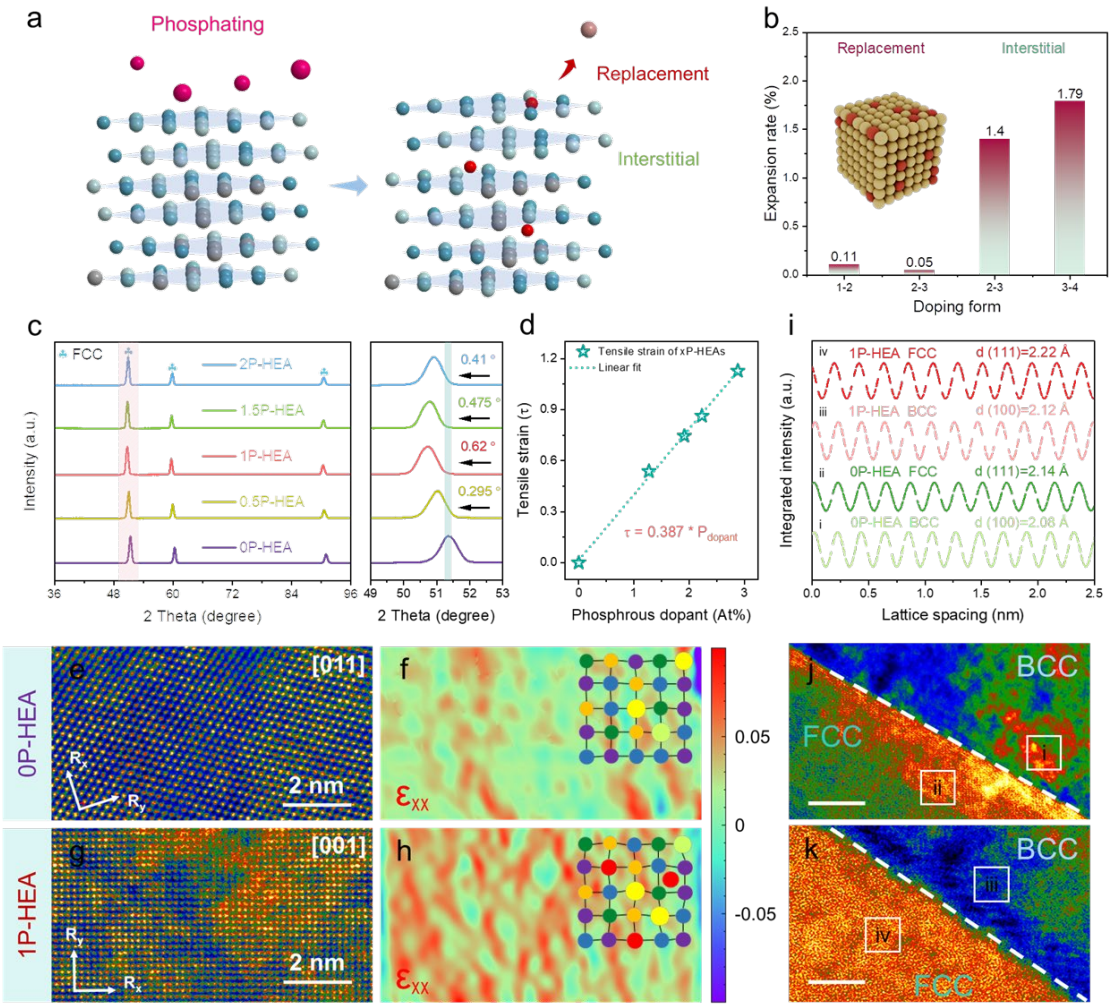

Figure 2. Simulation and characterizations of lattice strain in xP-HEAs via P doping strategy. (a) Simulation model of P doping process. (b) Calculated expansion rates induced by P doping. (c-d) XRD patterns and the calculated lattice strain as a function of the P composition. (e, g) HAADF-STEM images of 0P-HEA and 1P-HEA (on the surface), corresponding (f, h) strain maps (e_{xx}, along the [200] direction). (i) Interplanar spacing of 1P-HEA and 0P-HEA calculated by fast flourier transformation (FFT). (j-k) HRTEM images of 1P-HEA and 0P-HEA (in the matrix).

To understand the P doping induced structure evolution for HEA, simulations based on first-principles theory were conducted. As shown in Figure 2a, under the high-temperature and high-pressure conditions, atomic P tends to migrate and be doped in two ways, namely forming substitutional and interstitial atoms, respectively. Thermodynamically, the substitution of phosphorous for metal atoms preferentially

happens on the surface. And larger energy barrier needs to be overcome by substitution as the depth increases (Figure S16), thus P dopants are inclined to transform from substitutional to interstitial ones. As the dimension of the P atom is significantly larger than the FCC octahedral interstice (Table S6-S7), interstitial P atoms tend to cause lattice expansion while substitutional ones present far less expansion (Figure 2b), resulting in an uneven distribution of lattice strain along the depth profile. To verify this theorical prediction, ion thinning was utilized to expose various depths of 1P-HEA electrode and further characterized by XRD, as shown in Figure S17, which confirmed the gradient distribution of lattice strain.

As discussed above, the P element exists in both surface and matrix of P-HEAs, however, only FCC peaks with slight shift towards the low-angle region can be identified from the X-ray diffraction plots for xP-HEAs (Figure 1b and 2c), which shows that isolated phosphorous atoms bond with metallic HEA rather than forming a crystalline TMP phase. Interestingly, the three main diffraction peaks of 1P-HEA move slightly towards the low-angle region compared to the original porous HEA sample. To verify whether the shift originated from P doping induced lattice strain, XRD patterns for all the xP-HEAs samples in the enlarged scanning region of 4 thetas from 49° to 53° are compared. All those peaks can be indexed to the (111) lattice plane of FCC phase, and they all move slightly towards the low-angle region with different shifting angles. Specifically, the lattice strain (τ) of xP-HEAs can be calculated based on the following Equation: [30–32]

$$\tau = \left|\frac{a - \bar{a}}{\bar{a}}\right| \times 100\%$$

where a is the lattice distance of P-doped HEAs, $\bar{a}$ is that of 0P-HEA. Therefore, as shown in Figure 2d, the internal strains present a linear shape with P composition, which is consistent with the variation trend of the P loading with NaH_2PO_2 additions. In this regard, both P composition and lattice strain reach climax when 1 g NaH_2PO_2 was added (Figure S10), which are 2.88 at% and 1.13%, respectively.

Furthermore, Raman spectra were also obtained to investigate the surface states by detecting the intrinsic vibrations in chemical bonds between atoms. As shown in Figure

S18, compared to pure metallic 0P-HEA without distinguishable Raman signal, 0.5P-HEA and 1P-HEA samples both present obvious peaks in the range of 2581 cm^{-1} to 2461 cm^{-1}. More importantly, the peak shifting and broadening effects have been observed when higher P loading was introduced into xP-HEAs. Based on the phonon confinement model, the broken constraint system of conservation of momentum ($q \approx 0$) symmetry contribute to both the Raman displacement and band width[33]. As a result, it can be inferred that different magnifications of internal strain exist within these two samples. These findings clearly prove the successful introduction of heteroatoms and tensile strain on the surface of xP-HEAs[34].

To determine the stress origin and analyze the crystal structure of 1P-HEA on the surface, Cs-corrected TEM (Cs-TEM) was conducted. Figure 2e and 2g show the HAADF-STEM images of 0P-HEA and 1P-HEA viewed from the [011] and [001] directions, respectively. The random distribution of the contrast shown in the two HAADF images indicates a random distribution of the metal constituent elements, which also proves that the phosphorus infiltration process does not lead to the segregation of metal elements in the HEA[35]. The corresponding mappings of the lattice strains along [200] were determined by GPA, which already proved efficient in directly measuring the dislocations and strain distributions at the atomic scale[36–40], as shown in Figure 2f and 2h. It is evident that the 1P-HEA has a more extensive distribution of lattice tensile stains in comparison with the 0P-HEA[39,41]. Besides, interplanar spacing was obtained from HRTEM results (Figure S19) and the lattice constant was calculated by the cubic crystal interplanar spacing formula. Compared to porous HEA, 1P-HEA shows larger lattice constant fluctuation (Figure S20). The large variation of the lattice constant reflects severe lattice distortion, which is reasonable given that 1P-HEA contains elements of relatively larger differences in atomic radius[35] (Table S6).

Considering the unique 3D porous structure of 1P-HEA, to verify the extensive presence of P element and corresponding strain distribution, HRTEM was conducted to characterize the matrix of 1P-HEA, in which the eutectic dual-phase were divided obviously by the phase interface (Figure 2j and 2k). Figure 2i presents the integrated pixel intensities of 1P-HEA and 0P-HEA samples along FCC//(111) and BCC//(100)

spacing directions according to the collected HRTEM and FFT images (Figure S21). The averaged lattice spacings of FCC and BCC in the 0P-HEA are determined to be 2.14 and 2.08 Å, consistence with previous reports[22]. The intensity profile of 1P-HEA shows an averaged FCC//(111) lattice spacing of 2.22 Å, larger than that of 0P-HEA (2.14 Å), so the value of lattice strain for 1P-HEA in the matrix could be calculated by HRTEM data as approximately 2.78%. The enlarged strain may be caused by two phases coexisted with individually possessed lattice expansion ability, which leads to a conceivable mismatch in the phase interface and thus larger internal stress. Further XRD patterns collected at various depths (0, 50, 100, 150 μm) and corresponding calculated tensile strain (Figure S17) are consistent with this trend.

Considering all structural and compositional characterizations, it can be inferred that the P-doping induced incomplete phosphorization process can limit the metal-phosphorous bonding in the HEA matrix and thus the main chemical composition for P-HEA is metallic HEA but with unique interstitial P doping in the matrix and unsaturated surface metal-phosphorous bonding[42]. And the extra phosphorous atoms are embedded into the HEA lattice, contributing to lattice expansion and strain effects. Compared to traditional metal element selection to modulate the adjacent environment of active sites, the P doping strategy possesses greater potential as an efficient post-treatment method.

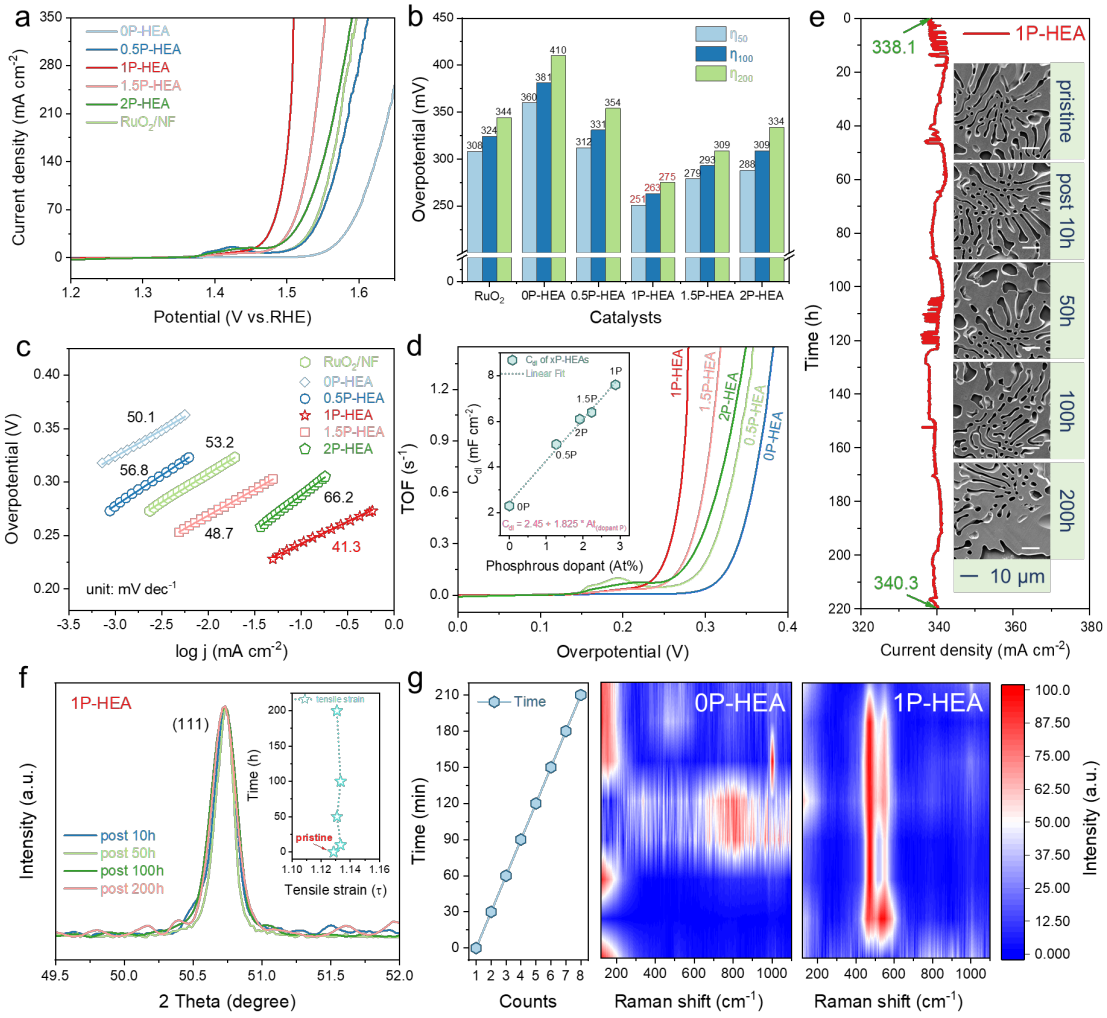

Figure 3. Electrochemical oxygen evolution reaction performance and study of the mechanism. (a) Linear sweep voltammetry (LSV) curves for xP-HEAs and RuO_2. (b) Overpotentials at specific current densities (50, 100, and 200 mA cm^{-2}). (c) Tafel plots. (d) Turnover frequency (TOF) curves. The inset is electrochemical double-layer capacitance (C_{dl}) values upon P content in xP-HEAs. (e) Stability testing of 1P-HEA via amperometric *i-t* curve. The insets are ex-situ SEM images before and after testing. (f) Ex-situ XRD patterns of 1P-HEA post a specific working period. The inset is calculated tensile strain upon operation time. (g) The time-dependent *in-situ* Raman spectra of 0P-HEA and 1P-HEA, the working potential is 1 V vs Ag/AgCl.

Since OER is a key obstruction step for electrochemical water splitting, we first evaluated the OER activity of the as-prepared electrodes in 1 M potassium hydroxide (KOH) aqueous solution at room temperature. The benchmark RuO_2 catalyst supported

on Ni foam (NF) was also included for comparison. Figure 3a presents the LSV curves of the samples. As for the 1P-HEA electrode, the current density increases rapidly with the increased overpotential, demonstrating remarkable OER performances. The 1P-HEA plate delivered an overpotential of 251, 263, and 275 mV at the current densities of 50, 100, and 200 mA cm^{-2} (normalized to the electrode area) (Figure 3b), respectively, superior to those of other counterparts and the benchmark RuO_2 electrode (308, 324 and 344 mV at the same current densities). As further compared with the current non-precious OER catalysts (Table S11), the 1P-HEA electrode shows competitive electrocatalytic performances.

To further investigate the OER kinetic, the Tafel plots calculated from the polarization curves are shown in Figure 3c. The Tafel slope of 1P-HEA is determined to be 41.3 mV dec^{-1}, much lower than that of non-doped 0P-HEA (50.1 mV dec^{-1}) and RuO_2 (53.2 mV dec^{-1}) catalysts. It indicates that the 1P-HEA proceeds with a faster OER kinetic than strain-less 0P-HEA. The ECSAs of xP-HEA catalysts are determined by their electrochemical double-layer capacitances[43]. The C_{dl} was calculated by testing CV curves in different scanning rates among the non-faradic current section (Figure S22). It is found that the C_{dl} value of 1P-HEA (7.6 mF cm^{-2}) is triple that of 0P-HEA (2.3 mF cm^{-2}), as shown in Figure S22a, demonstrating that more active sites could be exposed for 1P-HEA electrode, which allows for accelerated electrocatalytic reactions and electrolyte diffusions[44]. Moreover, a linear relationship between the P contents in xP-HEAs and the amount of exposed active sites was found (Figure 3d, inset), suggesting that P doping can improve the active site densities. Turnover frequency (TOF) was then calculated to assess the intrinsic OER activity quantitatively[45]. The 1P-HEA presents a TOF value of 1 s^{-1} at an overpotential of 277 mV (Figure 3d). This value is much higher than that of 0P-HEA, which is only 0.013 s^{-1} at the same overpotential. Comparisons of OER performances for xP-HEAs indicate that 1P-HEA electrode is superior to all the other HEA-based electrodes. Two main effects including strain and ligand effects introduced by the strain engineering strategy should be responsible for this perturbation. The internal strain differs among samples, thus enabling the possibility to regulate the intermediate adsorption strength[46–48], and the ligand effect

arises from the electronic structure of the binding metal atom which is affected by the surrounding metal atoms close to the binding site. The effect of a subsurface layer with guest P atoms has been observed to change the activity of the host atoms on the surface of HEA, as evidenced by XPS[49].

To understand the reaction mechanism and electronic structure during OER process, a theoretical study based on DFT calculations were also conducted. P-doped HEA and original HEA models (Figure S23) with elemental composition in consistence with experimental results were established. As shown in Figure S24, the free energy diagrams of HEA before and after P doping show that the P-doped HEA exhibits a lower Gibbs free energy change at rate-limiting step (OH*→ O) beyond no-doped HEA, illustrating that dopant P lowers the energy barrier. To further explore the electronic structure variation on the HEA surface before and after P doping process, the projected density of states (PDOS) with the O atom adsorption were investigated (Figure S25). The results demonstrate that after P doping, the density of states of the O 2p orbital emerges a sharp peak around -8 eV, suggesting that the energy of bonding effect of the O-surface increases, which could enhance the adsorption of O-containing intermediate and therefore facilitate the following reaction.

The stability curve of the 1P-HEA electrode (Figure 3e) shows no obvious degradation after 220 h testing, suggesting excellent mass transport and mechanical robustness properties in the OER process. Along with the stability testing, a series of ex-situ SEM images of 1P-HEA post a certain reaction time (10, 50, 100, and 200 h) were obtained and the well-kept porous morphology is observed, and also the post-reaction surficial strain was determined to maintain at 1.13% by ex-situ XRD patterns (Figure 3f), which is consistent with the post-reaction TEM results (Figure S26 and S27), suggesting the remarkable anti-corrosion and electrochemical stability properties of 1P-HEA under the anodic oxidation and caustic alkali condition. And LSV curve of the post-testing 1P-HEA electrode was also measured (Figure S28), and only 0.2% decay was found at the current density of 200 mA cm^{-2} compared to the pristine curve.

In-situ Raman measurements were conducted to monitor the operando structure self-

construction that occurred on the surface of 1P-HEA during the OER process. Figure S29 shows that 1P-HEA holds great structure stability even under a high working potential, while most of TMP-based electrocatalysts have been fully reconstructed rapidly. Long-term time-dependent Raman spectra reveal that there is no obvious peak of MOOH generated on 0P-HEA during the testing (Figure 3g). And 1P-HEA possesses two typical peaks of NiOOH species, located at 470 and 550 cm^{-1}, respectively, which could be attributed to the E_g bending vibration mode and the A_{1g} stretching vibration mode of Ni^{III}-O in NiOOH[50–52], respectively. However, the post-reaction XRD, XPS (Figure S30) and TEM confirm the low degree of reconstruction and high retention of strained layer.

To identify the real active site of 1P-HEA, we utilized *in situ* shielding method for shielding NiOOH species during the OER process[53,54]. The 10 mM KSCN is used to shield Ni, and the results show that the introduced shield reagent has a slightly negative effect on OER activity (9 mV increment at 100 mA cm^{-2}), but is still superior to that of 0P-HEA (Figure S31). However, no obvious decrease can be observed in the 0P-HEA, suggesting the excellent anti-poison of Ni/Co/Fe sites on the HEA and the poison of NiOOH sites is the main reason for activity loss (only 7.63% decay). Therefore, the ultra-thin layer of NiOOH species only has limited contribution to the promotion of OER activity and the strained 1P-HEA could still function as an outstanding “true catalyst”. And the roles of lattice strain and doping P played during the catalytic process remain a puzzle, a stress-relief annealing (SRA) method was taken to exclude the contribution of tensile strain. After SRA treatment, the strain on the surface of 1P-HEA disappeared (Figure S32) and the dopant P maintained its original content (Figure S33 and Table S3-S4), followed by the severe activity loss for both OER and HER processes (Figure S34), and the overpotential for 1P-HEA after SRA to achieve a current density of 100 mA cm^{-2} has risen to 321 mV (49.15% decay). Based on these results, it could be concluded that the dramatic enhancement of OER activity on 1P-HEA mainly benefits from the interaction between doping P and lattice strain, which not only increases the degree of atomic disorder thus facilizes the structural transformation process but also activates the intrinsic sites in the HEA thus leading to overall

promotion.

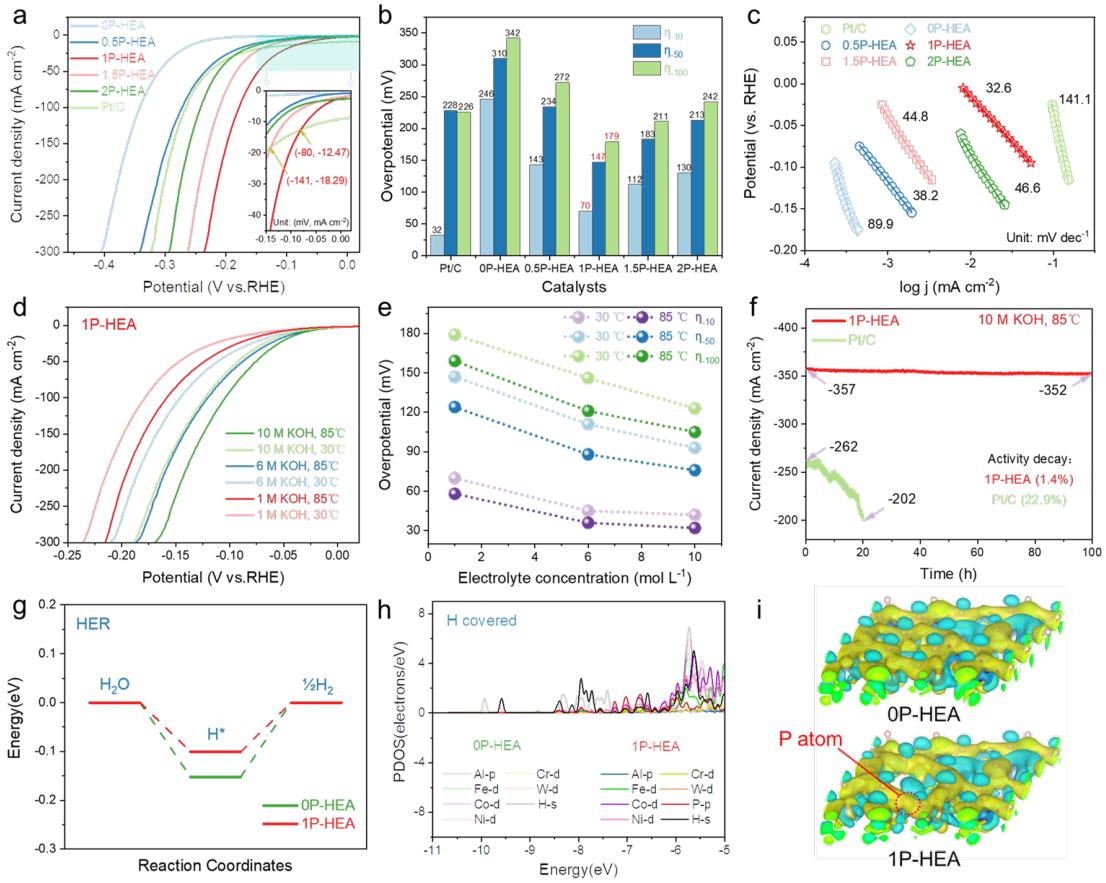

Figure 4. Electrochemical hydrogen evolution reaction performance and density function theory (DFT) calculations. (a) LSV curves for xP-HEAs. (b) Overpotentials at specific current densities of 10, 50, and 100 mA cm^{-2}. (c) Tafel curves. (d) LSV curves collected in various electrolytes. (e) Overpotential of 1P-HEA upon electrolyte concentration and working temperature. (f) Stability testing of 1P-HEA and Pt/C under industrial condition. (g) Free energy diagram of 0P-HEA and 1P-HEA. (h) Projected density of states (PDOS) of original and P-doped HEA after H adsorption. (i) Charge density difference of 0P-HEA and 1P-HEA after H adsorption. The areas of gain and loss of electrons are marked with yellow and cyan.

The HER activity and stability of the P-doped porous HEA catalysts were investigated and compared with commercial 20wt% Pt/C supported on NF. Figure 4a shows the LSV curves of P-doped HEA and 0P-HEA catalysts in N_2-saturated 1 M KOH. The 1P-HEA

displays an overpotential as low as 70 mV (Figure 4b) at the current density of 10 mA cm^{-2}, which is slightly higher than commercial Pt/C catalyst (32 mV) and surpasses the Pt/C at 80 mV. From Figure 4c, the Tafel slopes of 1P-HEA and 0P-HEA are 32.6 mV dec^{-1} and 89.9 mV dec^{-1}, respectively, which demonstrates the boosted HER kinetics. Moreover, the HER performance of 1P-HEA in various electrolytes is depicted in LSV curves (Figure 4d). The concentration of KOH in the electrolytes was chosen to be 6 M and 10 M, which are typical concentrations for industrial alkaline water splitting. An apparent trend is observed that the overpotentials of HER for 1P-HEA are decreasing along with the increment of electrolytes concentration and working temperature (Figure 4e). Notably, it takes only 32, 76, and 105 mV for 1P-HEA to achieve current densities of 10, 50, and 100 mA cm^{-2}, respectively.

The stability of the 1P-HEA electrode was checked via the *i-t* technique and repeated LSV testing in 1 M KOH solution (35℃). Figure S35a displays the LSV curves of 1P-HEA catalyst before and after 1000 times LSV cycles, exhibiting no apparent negative shift at the current density of 100 mA cm^{-2}. And after 100 h consecutive *i-t* testing (~345 mA cm^{-2}), no obvious degradation is found (Figure S35b), while the SEM images (Figure S36) of the 1P-HEA catalyst obtained after the stability test show that there is no morphology transformation occurred on the surface. Meanwhile, to further evaluate the stability of 1P-HEA and counterpart Pt/C catalysts, the *i-t* testing was conducted under industrial condition (10 M KOH, 85℃), and the result shows the remarkable activity retention of 1P-HEA and the poor stability of Pt/C (Figure 4f). These results further suggest the 1P-HEA delivers great potential in replacing commercial Pt/C towards industrial hydrogen generation.

DFT calculations were also deployed to study the HER performance of the P-doped HEA. As shown in Figure 4g, the HER energy barrier on the HEA surface after phosphating is reduced from 0.15 eV to about 0.1 eV. The addition of P atoms improves the efficiency of HER satisfactorily because the electrons in the P atoms occupy part of the HEA surface's bonding orbital and form a strong π bond with the d orbital of the metal atom, which leads to the weakening of the σ bonding between the H atom and the metal atom and makes the desorption of hydrogen easier. The above information can be

obtained from the dispersed P-2p orbital and the sharp H-1s orbital of P-doped HEA in Figure 4h[55]. After P doping, the density of states of the H-1s orbital below the Fermi level is shifted up (peaks near -10 and -6 eV), indicating that the energy of the bonding effect of the H-surface increases, which could also make the bonding more unstable. Although it is generally believed that the expansion of the lattice constant will lead to the upward shift of the d-band center of the surface metal atoms, which leads to an increase in the H adsorption energy, the study by Sung et al. pointed out that the d-band center model is not necessarily suitable for all situations and lattice expansion can also result in the weakening of the H adsorption energy[56], which is also confirmed in this work. The bonding competition effect of P and H atoms can also be observed from the charge density difference (Figure 4i). Normally, the electron cloud will transfer between two adjacent atoms to attract the nucleus thus forming an M-H bond. However, due to the existence of electronegative P atoms on the surface, a large number of electrons of the P and neighboring metal atoms will gather horizontally to cause the electron dissipation in the Z direction (cyan area) where H atoms might be located, thus weakening M-H interactions.

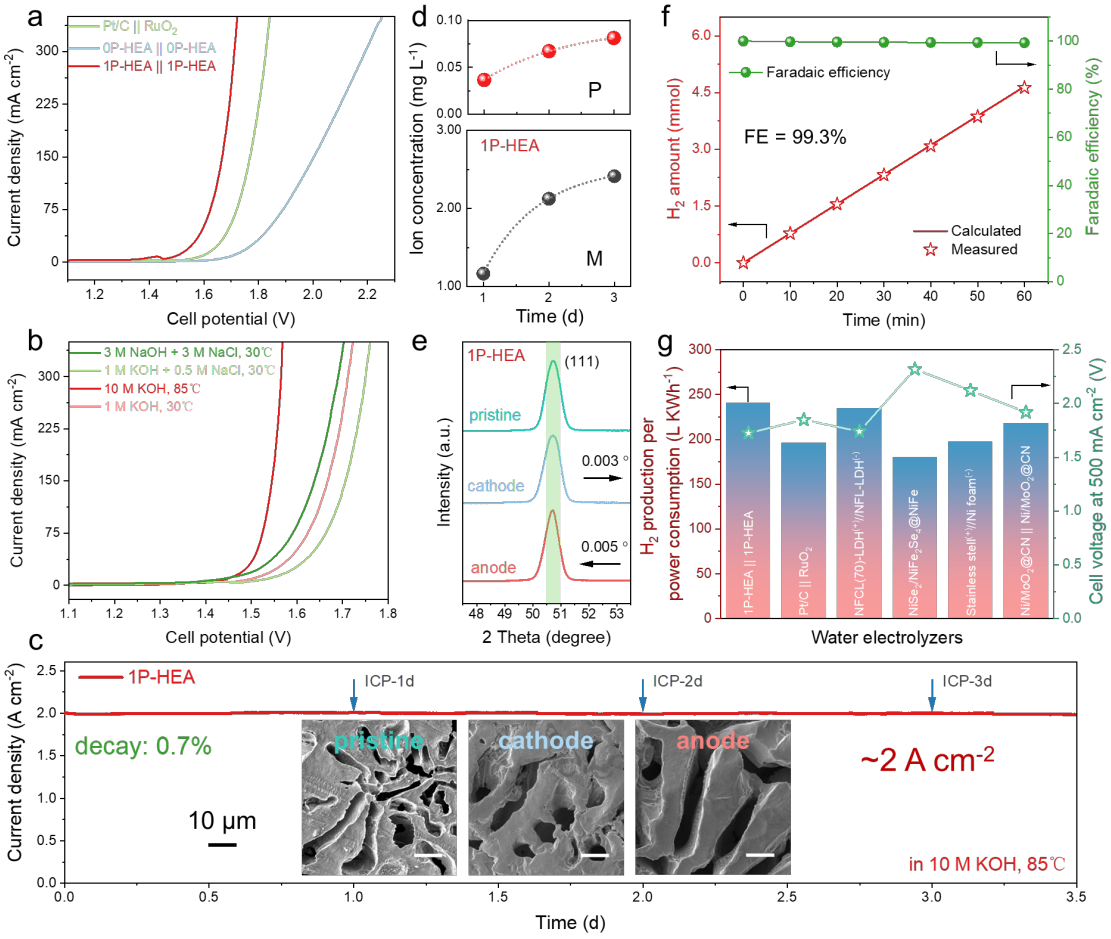

Figure 5. Overall water splitting (OWS) performance of as-constructed 1P-HEA || 1P-HEA electrolyzer. (a) LSV curves with a two-electrode configuration (laboratory condition). (b) LSV curves of 1P-HEA || 1P-HEA electrolyzer collected under different condition. (c) Long-term amperometric *i-t* curve at an industrial current density (~ 2 A cm^{-2}). The insets are the SEM images of 1P-HEA electrodes before and after long-term stability test. (d) Leached ion concentrations of P and metal elements in post-reaction electrolytes. (e) XRD patterns of 1P-HEA in different states. (f) Faradic efficiency (FE) of H_2 generation at 500 mA cm^{-2} in 1P-HEA || 1P-HEA electrolyzer upon operation time. (g) Hydrogen production per power consumption and cell voltages at 500 mA cm^{-2} of different electrolyzers[57–60].

Given that 1P-HEA exhibits excellent catalytic activities for both HER and OER, the full water splitting performance was further investigated in our experiment. A series of two-electrode water-splitting systems were constructed to test the overall performance.

For the electrolyzer based on 1P-HEA || 1P-HEA, 1P-HEA serves as both anode and cathode, while Pt/C and RuO_2 supported on NF function as cathode and anode respectively in the Pt/C || RuO_2 system. As shown in Figure 5a, an electrolyzer consisting of 1P-HEA || 1P-HEA shows the best performance for the OWS process. It takes only 1.51, 1.6, and 1.64 V of cell potentials for 1P-HEA || 1P-HEA to achieve specific current densities at 10, 50, and 100 mA cm^{-2}, much lower than the values of 1.6, 1.7, 1.74 V for Pt/C || RuO_2, and 1.71, 1.84, 1.93 V for 0P-HEA || 0P-HEA (Figure S37), respectively. Moreover, the 1P-HEA || 1P-HEA electrolyzer was further applied to various water splitting environments, and huge application potential was verified by the outstanding performance (Figure 5b). To be specific, the electrolyzer delivers a current density of 100 mA cm^{-2} at 1.53 V in industrial water splitting (10 M KOH, 85℃), 1.68 V in simulated alkaline sea-water (1 M KOH + 0.5 M NaCl, 30℃), and 1.61V in chlor-alkali (3 M NaOH + 3 M NaCl, 30℃) environments (Figure S38), and remain its high-activity after long-term stability testing in these electrolytes (Figure S39). These results suggest that 1P-HEA exhibits an enormous potential in sea-water electrocatalysis and the chemical industry for making chlorine and alkali.

To further verify the industrial potential of the 1P-HEA electrode to generate hydrogen, stability testing via the amperometric *i-t* technique was carried out at an ultrahigh current density of 2 A cm^{-2}. As shown in Figure 5c, 1P-HEA || 1P-HEA shows excellent electrochemical stability under the industrial condition, accompanied by large amounts of ceaseless bubbles. It demonstrates that the 3D porous structure of 1P-HEA not only avails the infiltration of reactants but also provides efficient diffusion channels which are convenient for the rapid release of gaseous products. Besides, the high stability of post-reaction 1P-HEA || 1P-HEA electrolyzer was also verified by the repeated LSV curves (Figure S40). Additionally, various characterizations were conducted to evaluate the structural and compositional stability of 1P-HEA electrodes. SEM images (Figure 5c, insets) for 1P-HEA electrodes before and after stability test demonstrate that there is no observable morphology change on the 1P-HEA electrodes surface. And ICP-OES results reveal negligible dissolution of composed elements in the post-reaction electrolytes, and the calculated total loss of P content ($m_{P\text{-}loss}$ / $m_{P\text{-}in\ HEA}$) is 0.53 % in

mass rate (Figure 5d and Table S5). And no apparent strain reduction on the surface of 1P-HEA electrodes is found, according to the XRD patterns shown in Figure 5e. The comprehensive stability of 1P-HEA under harsh condition in terms of morphology, composition, and structure may be attributed to the phase and thermal robustness of the HEA FCC solid solution.

To quantify the amount of generated H_2 through gas chromatography (GC), an H-cell construction was applied to conduct the OWS testing (Figure S41). The Faradaic efficiency for HER on the cathodic part in the 1P-HEA || 1P-HEA electrolyzer could be determined. The FE values at specific current densities (100, 200, 300, 400, and 500 mA cm^{-2}) were evaluated (Figure S42a), and the results show that 1P-HEA maintains a high FE value (> 99%) at the industrial current density. Long-term FE stability of 1P-HEA || 1P-HEA electrolyzer was measured (Figure 5f), and the stable value is calculated to be 99.3% (at 500 mA cm^{-2}), which is much higher than that of Pt/C || RuO_2 system (86.7% at the same current density, Figure S42b), demonstrating a great capability of 1P-HEA for H_2 production in the OWS application. Moreover, the efficiency of H_2 generation using various alkaline water electrolyzers is compared in Figure 5g, which demonstrates that the 1P-HEA || 1P-HEA electrolyzer in this work delivers a supreme electricity-H_2 conversion efficiency (240.7 L KWh^{-1}) at an industrial current density (500 mA cm^{-2}) among these advanced ones[57–60]. The enhanced overall water splitting performance of 1P-HEA can be originated from the interactions between doped P and HEA matrix. Specifically, the metastable state caused by the surface defects leads to the formation of high-energy surface structures, which can supply more active absorption sites for both HER and OER, and the formed internal lattice strain contributes to the charge redistribution and attractive interactions between the surface and bulk atoms, which further promotes charge separation[48]. In general, the introduction of P heteroatoms could induce tunable lattice strain in high entropy alloy crystals, serving as a promising strategy to promote the overall water splitting catalytic performance.

Conclusions

In conclusion, we introduce a novel strain engineering strategy for HEA via a tunable

doping route to improve its intrinsic catalytic activity for electrochemical overall water spitting. To be specific, external P atom doping and its induced graded tensile strain significantly influence the electronic structure of transition metal elements in the HEA, optimize intermediate absorption energy, and thus vastly promote HEA's full water splitting performance. Detailed experimental characterizations and DFT calculations have verified that atomic phosphorus induces tunable lattice strain in high entropy alloys, which value affects electrochemical performance dramatically. Compared with 0P-HEA and other xP-HEAs, the 1P-HEA electrode with the highest P doping content and largest internal tensile strain delivers the most favorable electrocatalytic activity towards water splitting and excellent stability under ultrahigh current density. Particularly, 1P-HEA requires overpotentials of 70 mV and 211 mV, respectively, to achieve a HER/OER current density of 10 mA cm^{-2}. Moreover, the 1P-HEA || 1P-HEA electrolyzer possesses much lower cell potential than its noble-metal counterpart. This work demonstrates the feasibility of tuning internal lattice strain in HEAs by facile doping route, and it could be potentially extended to other group V elements or other ions with different valences beyond P, thus paving a new way to construct the low-cost high-performance defect-rich bifunctional self-supporting electrode to be applied for industrial hydrogen production.

Acknowledgment

This work was funded by the National Natural Science Foundation of China (52002324), Natural Science Foundation of Chongqing (cstc2021jcyj-msxmX0471), Hong Kong Scholars Program (XJ2021039, PolyU YZ4V), Young Talent fund of University Association for Science and Technology in Shaanxi (20210401), China Postdoctoral Science Foundation (2020M683553), and Hong Kong RGC GRF (PolyU 15301121). We would like to thank the Analytical & Testing Center of Northwestern Polytechnical University for partial support on sample characterizations.

Additional information

The authors declare no conflict of interest.

Key words

high-entropy alloys, strain engineering, heteroatom doping, electrochemical water splitting, density function theory

References:

[1] R. C. Armstrong, C. Wolfram, K. P. De Jong, R. Gross, N. S. Lewis, B. Boardman, A. J. Ragauskas, K. Ehrhardt-Martinez, G. Crabtree, M. V. Ramana, *Nat. Energy* **2016**, *1*, 15020.

[2] N. Kittner, F. Lill, D. M. Kammen, *Nat. Energy* **2017**, *2*, 17125.

[3] J. Kibsgaard, I. Chorkendorff, *Nat. Energy* **2019**, *4*, 430.

[4] B. Zhang, Y. Zheng, T. Ma, C. Yang, Y. Peng, Z. Zhou, M. Zhou, S. Li, Y. Wang, C. Cheng, *Adv. Mater.* **2021**, *33*, 2006042.

[5] J. Wang, Y. Gao, H. Kong, J. Kim, S. Choi, F. Ciucci, Y. Hao, S. Yang, Z. Shao, J. Lim, *Chem. Soc. Rev.* **2020**, *49*, 9154.

[6] J. Song, C. Wei, Z. F. Huang, C. Liu, L. Zeng, X. Wang, Z. J. Xu, *Chem. Soc. Rev.* **2020**, *49*, 2196.

[7] J. Hou, Y. Wu, B. Zhang, S. Cao, Z. Li, L. Sun, *Adv. Funct. Mater.* **2019**, *29*, 1808367.

[8] J. Zhu, L. Hu, P. Zhao, L. Y. S. Lee, K. Y. Wong, *Chem. Rev.* **2020**, *120*, 851.

[9] J. Zhang, Q. Zhang, X. Feng, *Adv. Mater.* **2019**, *31*, 1808167.

[10] H. Sun, Z. Yan, F. Liu, W. Xu, F. Cheng, J. Chen, *Adv. Mater.* **2020**, *32*.

[11] G. Yang, Y. Jiao, H. Yan, Y. Xie, A. Wu, X. Dong, D. Guo, C. Tian, H. Fu, *Adv. Mater.* **2020**, *32*, 2000455.

[12] Y. Guo, T. Park, J. W. Yi, J. Henzie, J. Kim, Z. Wang, B. Jiang, Y. Bando, Y. Sugahara, J. Tang, Y. Yamauchi, *Adv. Mater.* **2019**, *31*, 1807134.

[13] N. Yao, P. Li, Z. Zhou, Y. Zhao, G. Cheng, S. Chen, W. Luo, *Adv. Energy Mater.* **2019**, *9*, 1902449.

[14] S.-H. Li, M.-Y. Qi, Z.-R. Tang, Y.-J. Xu, *Chem. Soc. Rev.* **2021**, *50*, 7539.

[15] Y. Shi, M. Li, Y. Yu, B. Zhang, *Energy Environ. Sci.* **2020**, *13*, 4564.

[16] H. Ding, H. Liu, W. Chu, C. Wu, Y. Xie, *Chem. Rev.* **2021**, *121*, 13174.

[17] D. Cao, D. Liu, S. Chen, O. A. Moses, X. Chen, W. Xu, C. Wu, L. Zheng, S. Chu, H. Jiang, C. Wang, B. Ge, X. Wu, J. Zhang, L. Song, *Energy Environ. Sci.* **2021**, *14*, 906.

[18] E. P. George, D. Raabe, R. O. Ritchie, *Nat. Rev. Mater.* **2019**, *4*, 515.

[19] H. Li, Y. Han, H. Zhao, W. Qi, D. Zhang, Y. Yu, W. Cai, S. Li, J. Lai, B. Huang, L. Wang, *Nat. Commun.* **2020**, *11*, 5437.

[20] Y. Xin, S. Li, Y. Qian, W. Zhu, H. Yuan, P. Jiang, R. Guo, L. Wang, *ACS Catal.* **2020**, *10*, 11280.

[21] B. R. Wygant, K. Kawashima, C. B. Mullins, *ACS Energy Lett.* **2018**, *3*, 2956.

[22] Q. Wu, Z. Wang, T. Zheng, D. Chen, Z. Yang, J. Li, J. jung Kai, J. Wang, *Mater. Lett.* **2019**, *253*, 268.

[23] X. Han, Q. Chen, Q. Chen, Q. Wu, Z. Xu, T. Zheng, W. Li, D. Cui, Z. Duan, J. Zhang, J. Li, H. Li, Z. Wang, J. Wang, Z. Xia, *J. Mater. Chem. A* **2022**, *10*, 11110.

[24] Z. Pu, T. Liu, I. S. Amiinu, R. Cheng, P. Wang, C. Zhang, P. Ji, W. Hu, J. Liu, S. Mu, *Adv. Funct. Mater.* **2020**, *30*, 2004009.

[25] S. A. Kube, S. Sohn, D. Uhl, A. Datye, A. Mehta, J. Schroers, *Acta Mater.* **2019**, *166*, 677.

[26] Y. Xu, X. Li, J. Gao, J. Wang, X. Wen, Y. Yang, Y. Li, M. Ding, *Science.* **2021**, *613*, 610.

[27] R. Boppella, J. Tan, W. Yang, J. Moon, *Adv. Funct. Mater.* **2019**, *29*, 1.

[28] M. Kuang, J. Zhang, D. Liu, H. Tan, K. N. Dinh, L. Yang, H. Ren, W. Huang, W. Fang, J. Yao, X. Hao, J. Xu, C. Liu, L. Song, B. Liu, Q. Yan, *Adv. Energy Mater.* **2020**, *10*, 2002215.

[29] W. Wang, Y. B. Zhu, Q. Wen, Y. Wang, J. Xia, C. Li, M. W. Chen, Y. Liu, H. Li, H. A. Wu, T. Zhai, *Adv. Mater.* **2019**, *31*, 1900528.

[30] Y. Wang, X. Li, M. Zhang, Y. Zhou, D. Rao, C. Zhong, J. Zhang, X. Han, W. Hu, Y. Zhang, K. Zaghib, Y. Wang, Y. Deng, *Adv. Mater.* **2020**, *32*, 200231.

[31] P. Strasser, S. Koh, T. Anniyev, J. Greeley, K. More, C. Yu, Z. Liu, S. Kaya, D. Nordlund, H. Ogasawara, M. F. Toney, A. Nilsson, *Nat. Chem.* **2010**, *2*,

454.

[32] M. Luo, S. Guo, *Nat. Rev. Mater.* **2017**, *2*, 17059.

[33] B. Huang, Y. Liu, Q. Pang, X. Zhang, H. Wang, P. K. Shen, *J. Mater. Chem. A* **2020**, *8*, 22251.

[34] Z. M. M. Ž. ć Snežzana Miljanić, Leo Frkanec, Tomislav Biljan, *J. Raman Spectrosc.* **2007**, *38*, 1538.

[35] Z. An, S. Mao, Y. Liu, L. Wang, H. Zhou, B. Gan, Z. Zhang, X. Han, *J. Mater. Sci. Technol.* **2021**, *79*, 109.

[36] M. H. Oh, M. G. Cho, D. Y. Chung, I. Park, Y. P. Kwon, C. Ophus, D. Kim, M. G. Kim, B. Jeong, X. W. Gu, J. Jo, J. M. Yoo, J. Hong, S. McMains, K. Kang, Y. E. Sung, A. P. Alivisatos, T. Hyeon, *Nature* **2020**, *577*, 359.

[37] Z. Li, Q. Wang, X. Bai, M. Wang, Z. Yang, Y. Du, G. E. Sterbinsky, D. Wu, Z. Yang, H. Tian, F. Pan, M. Gu, Y. Liu, Z. Feng, Y. Yang, *Energy Environ. Sci.* **2021**, *14*, 5035.

[38] S. Hao, H. Sheng, M. Liu, J. Huang, G. Zheng, F. Zhang, X. Liu, Z. Su, J. Hu, Y. Qian, L. Zhou, Y. He, B. Song, L. Lei, X. Zhang, S. Jin, *Nat. Nanotechnol.* **2021**, *16*, 1371.

[39] G. Liang, L. Yang, Q. Han, G. Chen, C. Lin, Y. Chen, L. Luo, X. Liu, Y. Li, R. Che, *Adv. Energy Mater.* **2020**, *10*, 1904267.

[40] S. Liu, Z. Hu, Y. Wu, J. Zhang, Y. Zhang, B. Cui, C. Liu, S. Hu, N. Zhao, X. Han, A. Cao, Y. Chen, Y. Deng, W. Hu, *Adv. Mater.* **2020**, *32*, 2006034.

[41] J. Deng, C. Wang, G. Guan, H. Wu, H. Sun, L. Qiu, P. Chen, Z. Pan, H. Sun, B. Zhang, R. Che, H. Peng, *ACS Nano* **2017**, *11*, 8464.

[42] H. Jin, X. Wang, C. Tang, A. Vasileff, L. Li, A. Slattery, S. Z. Qiao, *Adv. Mater.* **2021**, *33*, 20075081.

[43] Z. Gu, H. Shen, Z. Chen, Y. Yang, C. Yang, Y. Ji, Y. Wang, C. Zhu, J. Liu, J. Li, T. K. Sham, X. Xu, G. Zheng, *Joule* **2021**, *5*, 429.

[44] Y. H. Wang, W. J. Jiang, W. Yao, Z. L. Liu, Z. Liu, Y. Yang, L. Z. Gao, *Rare Met.* **2021**, *40*, 2327.

[45] M. Zhang, M. Wang, B. Xu, D. Ma, *Joule* **2019**, *3*, 2876.

[46] M. Escudero-Escribano, P. Malacrida, H. M. Hansen, U. Vej-Hansen, A. Velazquez-Palenzuela, V. Tripkovic, J. Schiøtz, J. Rossmeisl, I. E. L. Stephens, I. Chorkendorff, *Science.* **2016**, *352*, 73.

[47] A. Khorshidi, J. Violet, J. Hashemi, A. A. Peterson, *Nat. Catal.* **2018**, *1*, 263.

[48] L. Wang, Z. Zeng, W. Gao, T. Maxson, D. Raciti, M. Giroux, X. Pan, C. Wang, J. Greeley, *Science.* **2019**, *363*, 870.

[49] A. Holewinski, J. C. Idrobo, S. Linic, *Nat. Chem.* **2014**, *6*, 828.

[50] Q. Xu, H. Jiang, X. Duan, Z. Jiang, Y. Hu, S. W. Boettcher, W. Zhang, S. Guo, C. Li, *Nano Lett.* **2021**, *21*, 492.

[51] Y. Xie, Y. Sun, H. Tao, X. Wang, J. Wu, K. Ma, L. Wang, Z. Kang, Y. Zhang, *Adv. Funct. Mater.* **2022**, *32*.

[52] Y. Sun, J. Wu, Y. Xie, X. Wang, K. Ma, Z. Tian, Z. Zhang, Q. Liao, W. Zheng, Z. Kang, Y. Zhang, *Adv. Funct. Mater.* **2022**, *32*, 2207116.

[53] L. Yan, Y. Xu, P. Chen, S. Zhang, H. Jiang, L. Yang, Y. Wang, L. Zhang, J. Shen, X. Zhao, L. Wang, *Adv. Mater.* **2020**, *32*, 2003313.

[54] Q. Fan, P. Hou, C. Choi, T. S. Wu, S. Hong, F. Li, Y. L. Soo, P. Kang, Y. Jung, Z. Sun, *Adv. Energy Mater.* **2020**, *10*, 1903068.

[55] R. Hoffmann, *Angew. Chemie Int. Ed. English* **1987**, *26*, 846.

[56] S. Sakong, A. Groß, *Surf. Sci.* **2003**, *525*, 107.

[57] X. Lin, S. Cao, X. Chen, H. Chen, Z. Wang, H. Liu, H. Xu, S. Liu, S. Wei, X. Lu, *Adv. Funct. Mater.* **2022**, *32*, 2202072.

[58] J. Yuan, X. Cheng, H. Wang, C. Lei, S. Pardiwala, B. Yang, Z. Li, Q. Zhang, L. Lei, S. Wang, Y. Hou, *Nano-Micro Lett.* **2020**, *12*, 104.

[59] C. Liang, P. Zou, A. Nairan, Y. Zhang, J. Liu, K. Liu, S. Hu, F. Kang, H. J. Fan, C. Yang, *Energy Environ. Sci.* **2020**, *13*, 86.

[60] G. Qian, J. Chen, T. Yu, J. Liu, L. Luo, S. Yin, *Nano-Micro Lett.* **2022**, *14*, 20.